Single-valley engineering in graphene superlattices

Yafei Ren, Xinzhou Deng, Zhenhua Qiao, Changsheng Li, Jeil Jung, Changgan Zeng, Zhenyu Zhang, and Qian Niu

Phys. Rev. B **91**, 245415 — Published 15 June 2015

DOI: 10.1103/PhysRevB.91.245415

Single-Valley Engineering in Graphene Superlattices

Yafei Ren,[1,2] Xinzhou Deng,[1,2] Zhenhua Qiao,[1,2,*] Changsheng Li,[3] Jeil Jung,[4] Changgan Zeng,[1,2] Zhenyu Zhang,[1] and Qian Niu[5]

[1]*International Centre for Quantum Design of Functional Materials, Hefei National Laboratory for Physical Sciences at Microscale, and Synergetic Innovation Center of Quantum Information and Quantum Physics, University of Science and Technology of China, Hefei, Anhui 230026, China*
[2]*Department of Physics, University of Science and Technology of China, Hefei, Anhui 230026, China*
[3]*Department of Physics, Hunan University of Arts and Science, Changde, Hunan 415000, China*
[4]*Department of Physics, University of Seoul, Seoul, 130-743, Korea*
[5]*Department of Physics, The University of Texas at Austin, Austin, Texas 78712, USA*

The two inequivalent valleys in graphene are protected against long range scattering potentials due to their large separation in momentum space. In tailored $\sqrt{3}N \times \sqrt{3}N$ or $3N \times 3N$ graphene superlattices, these two valleys are folded into Γ and coupled by Bragg scattering from periodic adsorption. We find that, for top-site adsorption, strong inter-valley coupling closes the bulk gap from inversion symmetry breaking and leads to a single-valley metallic phase with quadratic band crossover. The degeneracy at the crossing point is protected by C_{3v} symmetry. In addition, the emergence of pseudo-Zeeman field and valley-orbit coupling are also proposed, which provide the possibility of tuning valley-polarization coherently in analogy to real spin for spintronics. Such valley manipulation mechanisms can also find applications in honeycomb photonic crystals. We also study the strong geometry-dependent influence of hollow- and bridge-site adatoms in the inter-valley coupling.

PACS numbers: 68.65.Cd, 71.10.Pm, 73.22.Pr, 73.43.Cd

I. INTRODUCTION

Honeycomb Dirac materials have two-fold degenerate band structures with inequivalent KK′ valleys,[1–5] whose origin can be traced back to the bipartite nature of honeycomb lattices (A and B triangular sublattices). This binary valley degree of freedom has led to proposals of valleytronics applications[6–12] that leverage the valley pseudospins in a manner analogous to electron spins in spintronics applications. A distinct scenario is that of single (odd-number) Dirac-cone in $\mathbb{Z}_2$ topological insulators[13] where their surface states are effectively decoupled from each other due to their distant spatial separation. Therefore, a single Dirac-cone structure is desirable when we require a Hamiltonian that embodies the chiral anomaly of Dirac fermions[14] and at the same time is protected against inter-valley scattering.

In this paper, we propose to engineer a single valley phase in 2D honeycomb Dirac materials through $\sqrt{3}N \times \sqrt{3}N$ or $3N \times 3N$ superlattices that fold and couple the inequivalent KK′ valleys into the same Γ. Utilizing the π-band tight-binding model and block-diagonalization method, we show that the effective Hamiltonian for top-site adsorbed superlattices exhibit inter-valley coupling and valley-orbit coupling mechanisms that resemble the conventional in-plane Zeeman fields and spin-orbit coupling of the electron spins.[1,2,15–20] The pseudo-Zeeman field and pseudospin-orbit coupling allow to control valley polarization coherently, while the latter one further indicates the possibility of manipulating valley polarization via electric fields. Moreover, together with the coexisting staggered sublattice potentials, we find that inter-valley coupling can drive a topological phase transition from a quantum valley-Hall phase into a single-valley metallic phase with quadratic band crossover. We also propose that such inter-valley coupling mechanism and quadratic band crossover can be observed in photonic crystals. Then we turn to study the inter-valley coupling mechanisms in hollow- and bridge-site decorated graphene and find that the inter-valley coupling mechanisms are strongly dependent on the adsorption geometry.

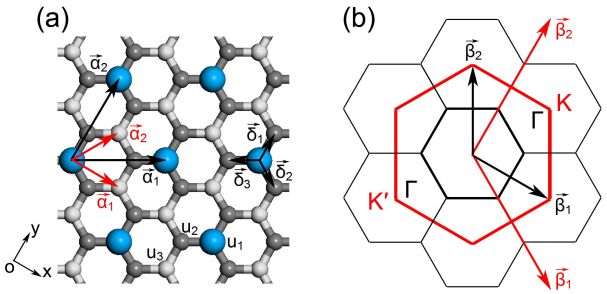

FIG. 1: (color online) Schematic representation of inter-valley coupling adatom superlattices and their respective Brillouin zones. (a) and (b) are respectively primitive and reciprocal lattices for the top adsorption in $\sqrt{3}\times\sqrt{3}$ graphene supercells. The red lines represent the Brillouin zone of pristine graphene.

The remainder of this paper is organized as follows. The inter-valley coupling of top-site adsorption and the topological phase transition are presented in Sec. II. The possible applications of the band-crossing phase are then discussed. The results of hollow and bridge adsorption

are shown in Sec. III and we present the summary in Sec. IV. Appendix A and B separately present the methods for calculating the photonic band structure and the symmetry analysis of three adsorption geometries.

II. TOP SITE ADSORPTION

A. Inter-valley coupling

When the $\sqrt{3}N \times \sqrt{3}N$ or $3N \times 3N$ supercells are tailored on a honeycomb lattice, KK′ valleys are coupled by Bragg scattering[21] since they are folded into Γ valley, as illustrated schematically in Fig. 1(b) showing the reciprocal lattices for both 1×1 (red) and $\sqrt{3} \times \sqrt{3}$ (black) supercells. Here, we only focus on the top-site adsorption in $\sqrt{3} \times \sqrt{3}$ supercell as shown in Fig. 1(a) where the six atoms in each primitive cell can be classified into three different categories: (i) one at the adatom site, (ii) three at the nearest neighbor sites, and (iii) two at next-nearest sites. We represent the corresponding site energies as u_1, u_2, and u_3, and set $u_3 = 0$ as the reference value. Assuming that the adsorption sites belong to sublattice "A", the real-space tight-binding Hamiltonian can be written as:

$$H_{\rm t} = H_0 + u_1 {\sum_i}' a_i^\dagger a_i + u_2 {\sum_i}' \sum_\delta b_{i+\delta}^\dagger b_{i+\delta}, \qquad (1)$$

where $\sum_i{}'$ runs over all adatom sites and $a_i^\dagger$ ($b_i^\dagger$) is the creation operator of an electron at i-th A(B) site. Here $H_0 = -t_0 \sum_{<ij>} (a_i^\dagger b_j + h.c.)$ is the band Hamiltonian of pristine graphene with t_0 being the nearest-neighbor hopping energy.

The Brillouin zone of pristine graphene can be represented through three copies of $\sqrt{3} \times \sqrt{3}$ graphene supercell's first Brillouin zone as displayed in Fig. 1(b). The three copies are set to be centered at $\mathbf{K}_j$ (j=1-3) that are respectively wavevectors of K, K′, and Γ points. Therefore, the operator a_i can be expanded in momentum space as: $a_i = \frac{1}{\sqrt{N_0}} \sum_{\boldsymbol{k}} \sum_j \exp[i(\mathbf{K}_j + \boldsymbol{k}) \cdot \mathbf{R}_i] a_{j,k}$, where N_0 is a normalization factor, and $\boldsymbol{k}$ runs over the first Brillouin zone of $\sqrt{3} \times \sqrt{3}$ graphene supercell. Then the Hamiltonian of Eq. (1) can be expressed in momentum space as:

$$H_{\rm t}(\boldsymbol{k}) = H_0(\boldsymbol{k}) + \sum_{j,j'} [\frac{u_1}{3} a_{j,k}^\dagger a_{j',k} + \frac{u_2}{3} \xi_{jj'} b_{j',k}^\dagger b_{j,k}], \quad (2)$$

where $H_0(\boldsymbol{k}) = -t_0 \sum_j (\chi_{jk} a_{j,k}^\dagger b_{j,k} + h.c.)$ describes the kinetic energy of pristine graphene with $\chi_{jk} = \sum_\delta e^{i(\mathbf{K}_j + \boldsymbol{k}) \cdot \boldsymbol{\delta}}$, and $\xi_{jj'} = \sum_\delta e^{i(\mathbf{K}_j - \mathbf{K}_{j'}) \cdot \boldsymbol{\delta}}$. The last two terms give sublattice potentials when $j = j'$ which are different for AB sublattices due to inversion symmetry breaking. When $j \neq j'$, they give rise to inter-valley coupling through a finite u_1 contribution while u_2 contribution vanishes due to the phase interference (ξ_{12}=0). By block diagonalization, the low-energy effective Hamiltonian can be further obtained:

$$\begin{aligned} H_{\rm t}^{\rm eff} &= U_0 + v_F(\tau_z k_x \sigma_x + k_y \sigma_y) + \Delta_1 \sigma_z \qquad (3) \\ &+ \frac{\Delta_2}{2}(1 + \sigma_z)\tau_x, \end{aligned}$$

where U_0=$(\Delta_2 + u_2)/2$ and Δ_1=$(\Delta_2 - u_2)/2$ with Δ_2=$u_1/3$. $\boldsymbol{\tau}$ and $\boldsymbol{\sigma}$ are respectively Pauli matrices of KK′ valleys and AB sublattices. The third term reflects the effective potential imbalance through a mass term of magnitude Δ_1 and the last term describes inter-valley coupling through the τ_x operator. We note that the coupling between K and K′ valleys only occurs at "A" sublattice with the coupling amplitude Δ_2 depending on u_1 linearly. Such an inter-valley coupling acts on the valley pseudospin as an effective Zeeman field that can be used to control the valley polarization coherently in valleytronics devices.

When the nearest neighbor hopping terms of superlattice Hamiltonians are allowed to change by $\delta t = t - t_0$ due to the influence of the adatoms, the real-space tight-binding Hamiltonian in Eq. (1) acquires an additional term $H' = {\sum_{\langle i,j \rangle}}' \delta t (a_i^\dagger b_j + h.c.)$ where the index i runs over "A" sites right underneath the adatoms and the j sites represent the three nearest "B" sites. The modified effective Hamiltonian becomes:

$$\begin{aligned} H_{\rm t}^{\rm eff\prime}(\boldsymbol{k}) &= U_0' + v_F'(\tau_z k_x \sigma_x + k_y \sigma_y) + \Delta_1' \sigma_z \mathbf{1}_\tau \\ &+ \frac{\Delta_2'}{2}(\mathbf{1}_\sigma + \sigma_z)\tau_x + v_\delta \sigma_y (\tau_y k_x + \tau_x k_y), \quad (4) \end{aligned}$$

where (U_0', Δ_1') have same forms as (U_0, Δ_1) by changing Δ_2 to be $\Delta_2' = 3u_1 t_0^2/(t + 2t_0)^2$, and the Fermi velocity is modified to be $v_F' = v_F(2t + t_0)/(t + 2t_0)$. The last term in Eq. (4) can be identified as a valley-orbit interaction of strength $v_\delta = v_F(t - t_0)/(t + 2t_0)$ coupled with a sublattice-flip potential. This term also couples different valleys and implies the possibility of manipulating the valley degree of freedom by external electric field in a manner analogous to the control of electron spin by electrical means via spin-orbit coupling.

B. Single-valley metallic phase

Adatom superlattices lead to both inter-valley coupling and inversion symmetry breaking potentials. It is easy to understand that each term can independently contribute in opening a Dirac point gap when they are viewed as uniform in-plane xy and out-of-plane z contributions to the pseudospin fields in the Dirac Hamiltonian,[22] where the former shifts the position of the Dirac points in momentum space and the latter introduces an inversion symmetry breaking gap in the Dirac cones. Here we show that when those effects are present simultaneously in a superlattice, a topologically distinct single-valley phase can be engineered. We begin considering for sake of clarity the top-adsorption configurations neglecting the

modification of the hopping energy in the band Hamiltonian and setting the site energies at all "B" sublattices to an assumed constant value (*i.e.*, $U_B = u_2 < 0$). When $u_1 = 0$, the site energies at all "A" sublattices are identical, *i.e.*, $U_A = 0$. This leads to vanishing inter-valley coupling and the imbalanced sublattice potentials open a quantum valley-Hall gap at the Dirac points, where the doubly-degenerate massive Dirac cones are folded as a single valley around the Γ point but remain distinguishable [See Fig. 2(a)]. When we allow u_1 to take negative values, we find a gradual decrease of the inversion symmetry breaking induced gap $|\Delta_1|$ and an increase of inter-valley coupling strength $|\Delta_2|$ that lifts the degeneracy of the conduction bands splitting by a magnitude of $2\Delta_2$ [See Fig. 2(b)]. The simultaneous presence of both terms breaks the particle-hole symmetry and leads to a smaller bulk gap $\Delta' = |2\Delta_1 + \Delta_2|$. However, the degeneracy of valence band edge is also present since it is protected by C_{3v} symmetry [See Appendix B].

When u_1 is even further decreased and reaches a critical value of $u_1 = 3u_2/2$, the bulk gap Δ' completely closes as shown in Fig. 2(c). Here we achieve a single band touching point at Γ formed by a Dirac-cone centered at the edge of the parabolic valence band. In this limit where the bulk gap is closed, the valley-Hall effect is absent and the valleys are no longer distinguishable. When we allow even smaller values of u_1, the inter-valley coupling strength $|\Delta_2|$ further increases, while the magnitude of the staggered sublattice potentials $|\Delta_1|$ first decreases to zero then increases again. During this process, a conduction-valence band inversion happens due to the strong inter-valley coupling and the doubly degenerate valence-band edges are split by a local band gap of $\Delta' = \Big|2|\Delta_1| - |\Delta_2|\Big|$ as displayed in Fig. 2(d). This band inversion drives the C_{3v} protected degenerate valence-band edges into a crossing point between conduction and valence bands producing a valley-mixed metallic phase with quadratic band crossover.

A detailed analysis of the band crossover at low energy limit shows that, when $|\Delta_2| \gg |\Delta_1|$, the low-energy Hamiltonian of the quadratic touching bands can be further simplified as:

$$H_{\rm t}^{\rm eff\,\prime\prime}(\boldsymbol{k}) \;=\; U_0'' + \alpha k^2 - \beta \begin{bmatrix} 0 & (\pi^\dagger)^2 \\ \pi^2 & 0 \end{bmatrix}, \qquad (5)$$

which is represented on the basis of "B" sublattice from both K and K′ valleys. Here, we define $U_0'' = U_0 - \Delta_1$, $k^2 = k_x^2 + k_y^2$, $\alpha = \Delta_1 v_F^2/(\Delta_2^2 - \Delta_1^2)$, and $\beta = \Delta_2 v_F^2/(\Delta_2^2 - \Delta_1^2)$. The last term couples states between valleys K and K′ with $\pi = k_x + ik_y$, and gives rise to the quadratically dispersing Fermi point band structure in analogy to bilayer graphene. However, an additional term, *i.e.*, αk^2, is present due to the inversion symmetry breaking which breaks the chiral symmetry and makes the low-energy bands different from that of bilayer graphene at K or K′ valley.

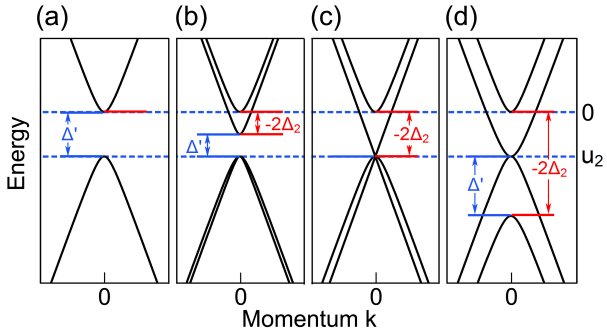

FIG. 2: (color online) Topological transition from a quantum valley-Hall insulator to a single-valley phase as a function of the parameters u_1. Here, we set u_2 to be fixed with $u_2 < 0$ and $u_3 = 0$. $-2\Delta_2$ corresponds to the local band gap from the inter-valley scattering. Δ' measures the bulk (local) band gap from the competition between inter-valley coupling and sublattice potentials. The progressive decrease of u_1 leads to a complete closure of the quantum valley-Hall gap and then transitions to the single valley phase by reversing Δ'.

C. Quadratic band crossover

Apart from the chiral symmetry breaking, the main difference between this band crossover and that of bilayer graphene is that here we have only a *single* parabolic dispersion. This is of interest, because it provides an ideal platform to study the single Dirac-cone transport phenomena of $\mathbb{Z}_2$ topological insulators and allows to explore the chiral anomaly of single valley physics that is not compensated by its time-reversal counterpart. For example, if broken symmetry gapped phases are developed in the presence of electron-electron interactions,[24–26] a mass sign dependent spontaneous orbital moments will develop per spin-valley.[26–28] In our single valley phase, it is expected that when the Fermi surface lies at the crossing point, a quantum anomalous Hall ground state will develop when both spin components have the same mass, or alternatively a quantum spin-Hall state will be present when the masses for each spin term have opposite signs.[29] Besides, a superconducting phase can also be expected when the Fermi surface is shifted away from the crossing point.[30] Whereas the energetically favored ground state depends on details of the band Hamiltonian and the models for the electron-electron interaction, further control of quantum phase transitions should be achievable by means of external magnetic fields coupling with the spontaneous orbital moments. Furthermore, in bilayer graphene, the magnitude of the gaps predicted in a Hartree-Fock theory without dynamical screening is on the order of a few tens of meV[26] whereas experimental gaps turned out to be an order of magnitude smaller ~ 2 meV[31] due to the exponentially increasing screening feedback when the gaps are small. Thus, it is expected that substantially larger gaps can develop, if flatter bands can be tailored when the leading parabolic dispersion coefficients can be made smaller than the one used in bilayer

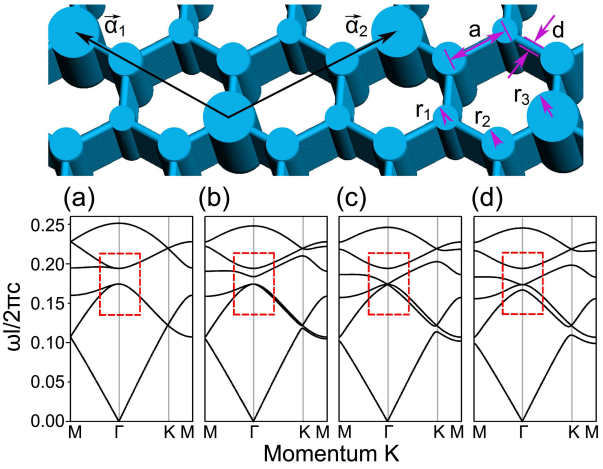

FIG. 3: (color online) Upper panel: Schematic representation of honeycomb photonic crystals with a $\sqrt{3} \times \sqrt{3}$ periodicity. $\vec{\alpha}_1$ and $\vec{\alpha}_2$ denote the primitive vectors. The distance between nearest columns is set to be a and the slab width is $d = 0.1a$. r_i (i = 1-3) label the radii of different columns. In our simulation, each column is chosen to be infinitely long. Lower panel: Photonic band structures of transverse-magnetic modes along high-symmetry lines for different radii $r_1 = 0.18a$ (a), $0.23a$ (b), $0.28a$ (c), and $0.32a$ (d), respectively. Here, we set $r_2 = 0.25a$ and $r_3 = 0.18a$.

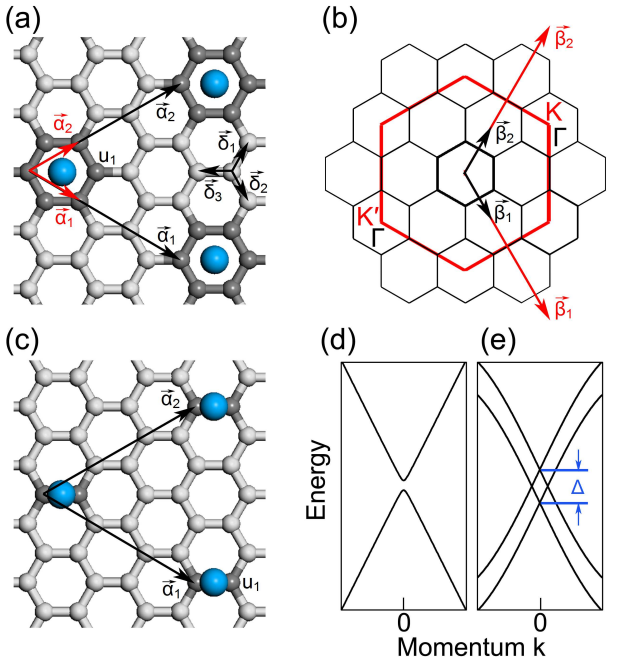

FIG. 4: (color online) Primitive cells for hollow- (a) and bridge-site (c) adsorption. $\vec{\alpha}_i$ indicates the primitive lattice vectors for 1×1 (in red) and 3×3 (in black) graphene supercell. u_1 denotes the site-energy induced by the adatoms. (b): Reciprocal lattices for 1×1 (in red) and 3×3 (in black) graphene supercell. (d) and (e): Low energy band structures for hollow- and bridge-site adsorptions. Δ indicates the local gap from pseudo-Zeeman field in bridge adsorption.

graphene. Moreover, in the presence of strong magnetic field, the anomalous Landau-level quantization can also be expected as that in bilayer graphene case.[32]

D. Photonic-crystal bands

Experimental realizations of periodic graphene superlattices could take advantage of substrates that can generate the 3×3- or $\sqrt{3} \times \sqrt{3}$-type superstructure, like EuO(111)[33] and Ag(111) substrates.[34] There are also other methods for engineering such kind of superstructures, *e.g.*, silicene on Ag(111) substrate,[35] InSb(111) surface,[36] artificial organic molecular lattice,[37] or patterned two dimensional electron gas with well-established experimental technique.[38] The applicability of our theory depends on the degree of the achievable commensurability with the crystal structure of honeycomb lattices. It is noteworthy that, since our model is spin independent, it can also apply to Bosonic systems like cold atoms[39] or photonic crystals[40] in honeycomb superlattices. One possibility is to use honeycomb photonic crystals made of silicon columns linked by thin silicon slabs as shown in the upper panel of Fig. 3, and use electromagnetic waves with transverse-magnetic modes in the xy plane. The corresponding site potentials and hopping energies for the photonic crystal setup can be controlled through the column radius r and the link width d. The confinement radii allow to tune the concentration of electrical-field energy of the harmonic modes.

If the columns' radii are identical and the connecting slabs have the same width, the two dimensional photonic band structure for transverse-magnetic modes[23] obtained from the finite elements method[41,42] shows two linearly dispersing Dirac cones, closely resembling the band structure of pristine graphene.[23,40,43] To model the $\sqrt{3} \times \sqrt{3}$ graphene supercell, we first classify the columns' radii into three categories r_i (i=1-3) with $r_3 = 0.18a$ as a reference, and the link width is chosen to be $d = 0.10a$ with a being the distance between two nearest columns. Figures 3(a)-3(d) display the photonic band structures for different $r_1 = 0.18a$ (a), $0.23a$ (b), $0.28a$ (c), and $0.32a$ (d) at fixed $r_2 = 0.25a$ along high symmetry lines. One can observe a topological phase transition from an insulator to a single-valley metallic phase when r_1 is progressively increased [See the highlighted regions] in a way closely similar to the behavior of the electronic band structure shown in Fig. 2.

III. HOLLOW AND BRIDGE ADSORPTION

In this part, we present the inter-valley coupling mechanisms for hollow and bridge adsorption in 3×3 honeycomb supercells as shown in Figs. 4(a) and 4(c). For both cases, the inversion symmetry is preserved and thus staggered sublattice potential is absent, which is differ-

TABLE I: Inter-valley coupling mechanisms for different adsorption sites.

Adsorption Site	Symmetry	Inter-Valley Coupling
Top	C_{3v}	$(1+\sigma_z)\tau_x$
Hollow	C_{6v}	$\tau_x\sigma_x$
Bridge	C_{2v}	$\tau_x\mathbf{1}_\sigma$

ent from top adsorption. The corresponding first Brillouin zones for pristine graphene and graphene supercells shown in Fig. 4(b) in red and black respectively where K and K′ points of pristine graphene are also folded into Γ inducing inter-valley coupling.

We first study the hollow adsorption as shown in Fig. 4(a). By considering only the site energies surrounding the adatoms, the real-space π-orbital tight-binding Hamiltonian is written as:

$$H_{\rm h} = H_0 + u_1 {\sum_i}' (a_i^\dagger a_i + b_i^\dagger b_i), \tag{6}$$

where $\sum_i'$ runs over six atoms nearest to adatoms with site energy of u_1. Since the Brillouin zone of pristine graphene can be divided into nine copies of that of 3×3 graphene supercell, the operator a_i can be expanded in momentum space as: $a_i = \frac{1}{\sqrt{N_0}}\sum_{\boldsymbol{k}}\sum_j \exp[-i(\mathbf{K}_j+\boldsymbol{k})\cdot\mathbf{R}_i]a_{j,k}$, where $\mathbf{K}_j$ (j = 1-9) denotes the center of j-th copy and $\boldsymbol{k}$ runs over the Brillouin zone of 3×3 graphene supercell. Therefore, the Hamiltonian of Eq. (6) in momentum space can be expressed as:

$$H_{\rm h}(\boldsymbol{k}) = H_0(\boldsymbol{k}) + \sum_{j,j'}\frac{u_1}{9}\xi_{jj'}(a_{j,k}^\dagger a_{j',k} + b_{j',k}^\dagger b_{j,k}). \tag{7}$$

In the second term, $j=j'$ gives equivalent AB sublattice potentials, while $j\neq j'$ couples different parts. Although the direct coupling between valleys KK′ vanishes due to phase interference, *i.e.*, $\xi_{12}=\sum_\delta e^{i(\mathbf{K}-\mathbf{K}')\cdot\boldsymbol{\delta}}=0$, a band gap opens at Γ point with four lower energy bands around the gap mainly contributed from eigenstates near valleys KK′ as shown in Fig. 4(d). This suggests that the gap is induced by inter-valley coupling from higher-order effects. By doing a block diagonalization,[44] a low-energy effective Hamiltonian with nontrivial contribution from u_1 can be obtained:

$$H_{\rm h}^{\rm eff} = \frac{u_1}{3} + v_F(\tau_z k_x\sigma_x + k_y\sigma_y) + \frac{u_1^2}{9t_0}\tau_x\sigma_x, \tag{8}$$

where the first term is an energy shift relative to the charge neutrality point. The last term couples valleys K and K′ where τ_x implies a pseudo-Zeeman field in x-direction to induce a precession of valley polarization. Moreover, the coupling only occurs between different sublattices, and the resulting band gap $2u_1^2/9t_0$ indicates a second-order correction from site energy u_1.

Then we turn to the bridge adsorption case as shown in Fig. 4(c). Assuming that the adatom only influences the site energies u_1 of the nearest two carbon atoms and neglecting the high-order contribution from Γ valley of graphene, the continuum effective Hamiltonian for four lower bands can be obtained similar to hollow adsorption, which can be expressed as follows:

$$H_{\rm b}^{\rm eff} = \frac{u_1}{9} + v_F(\tau_z k_x\sigma_x + k_y\sigma_y) + \frac{u_1}{9}\tau_x\mathbf{1}_\sigma. \tag{9}$$

where the third term represents the first-order inter-valley coupling contributed from the on-site energy, which also acts as a pseudo-Zeeman field in x-direction yet without a sublattice flipping. This term shifts the two degenerate Dirac cones of graphene and opens a local energy gap $\Delta = 2|u_1|/9$ at $\boldsymbol{k}=0$ as shown in Fig. 4(e). The gap is closed at $(\pm|u_1|/9v_F, 0)$ due to the dispersion of energy bands where another two Dirac cones are formed.

IV. DISCUSSIONS AND CONCLUSIONS

In summary, we presented the theory for the inter-valley coupling mechanisms due to Bragg scattering in $\sqrt{3}\times\sqrt{3}$ or 3×3 adatom decorated graphene supercells that act as in-plane pseudo-Zeeman fields or pseudospin-orbit coupling. Three possible adsorption geometries, *i.e.*, top-, hollow-, and bridge-site adsorption, are studied and we found that inter-valley coupling mechanisms are sensitive to the adsorption site as summarized in Table I. These inter-valley coupling mechanisms can be used to tailor valley pseudospins of honeycomb lattices and have important implications in valleytronics, where the coherent control of valley polarization is yet a grand challenge due to the missing counterpart mechanisms of spin-orbit couplings or magnetic fields for spintronics. Especially, the valley-orbit coupling in top adsorption case makes it possible to control the valley polarization via electric means. Moreover, our theory also suggests strategies for engineering single-valley electronic structure in conventional Dirac materials with two inequivalent degenerate valleys by folding them together. In addition, the single-valley phase for top adsorption can be manipulated by combining inter-valley couplings and imbalanced sublattice potentials originated from the inversion-symmetry breaking. By increasing the strength of inter-valley coupling from zero, a topological phase transition can take place from the quantum valley-Hall phase to a chiral anomalous single-valley metallic phase with quadratic band crossover that resemble the electronic structure of a *half* Bernal-stacked bilayer graphene apart from a chiral symmetry breaking term. A concrete proposal for such a single-valley phase is presented in honeycomb photonic crystals since a spinless particle is considered in the present work. When the spin degree of freedom is further included in the honeycomb structure (*e.g.*, silicene[45]), the competition between valley-mixing and spin-mixing mechanisms will give rise to a rich variety of topological phases, which is beyond the scope of the present work and will be discussed in our future work.

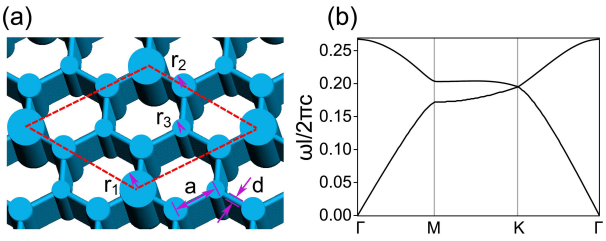

FIG. 5: (color online) Left panel: Schematic of honeycomb-structured photonic crystals. The distance between nearest columns is set to be a and the slab width is $d = 0.1a$. r_i (i = 1-3) label the radii of different columns. Right panel: The photonic band structure with uniform column radii and the slab widths where Dirac cones are present around K point and K$'$ point and the later one is not shown for clarity of the figure.

It is noteworthy that Ref. [46] presents similar inter-valley coupling terms. However, the physical origin of inter-valley coupling in our work is totally different from theirs, which comes from the short-range components of scattering potential from single adatom on graphene rather than Bragg scattering in graphene superlattice. In addition, when the supercell slightly deviates from the perfectly commensurate $\sqrt{3} \times \sqrt{3}$ supercell, the two inequivalent Dirac cones are preserved and remain separate although an inter-valley coupling gap can appear at higher energies due to the coupling between states away from K and K$'$ points as discussed in Ref. [47].

Acknowledgments

We acknowledge financial support from 100 Talents Program of Chinese Academy of Sciences, NNSFC (11474265, 11104069 and 11034006), DOE (DE-FG03-02ER45958) and Welch Foundation (F-1255). J.J. thanks the support from National Research Foundation of Singapore under its Fellowship program (NRF-NRFF2012-01). Q.N. is also supported by NBRPC (2012CB921300 and 2013CB921900), and NNSFC (91121004) during his leave at Peking University. The supercomputing center of USTC is acknowledged for computing assistance.

Appendix A: Calculation of Photonic Band Structure

In our simulation of photonic band structure, we consider a honeycomb lattice with $\sqrt{3}\times\sqrt{3}$ periodicity, which is comprised of silicon columns linked with thin silicon slabs in the vacuum background as shown in Fig. 5(a). The columns are infinite in z-direction and their radii are r_i (i = 1-3). In our calculation, the electromagnetic wave propagates within the xy plane, *i.e.*, the wavevector component along z-direction is $k_z = 0$. Various numerical methods can be used to calculate the photonic band structure, such as plane wave method (PWE), finite difference time domain (FDTD) method, and finite elements method (FEM).[41,42] Here, FEM is employed, which is much efficient in calculating structures with extremely small domains needing to be meshed. The photonic band structure with the uniform column radii and the slabs widths are calculated as shown in Fig. 5(b), where two Dirac cones in K and K$'$ points for transverse-magnetic modes[40,43] are formed, resembling the linear-dispersed Dirac cones of pristine graphene.

Appendix B: Symmetry Analysis

In this part, we derive the inter-valley coupling mechanisms utilizing symmetry analysis. We focus on the Hilbert space spanned by four basis functions: $|K_A\rangle$, $|K_B\rangle$, $|K'_A\rangle$, and $|K'_B\rangle$ defined as below

$$\begin{aligned}
|K_A\rangle &= \frac{1}{\sqrt{N}}\sum_i e^{i\mathbf{K}\cdot[\mathbf{R}_i+\boldsymbol{\tau}_A]}|p_z,i,A\rangle \\
|K_B\rangle &= \frac{1}{\sqrt{N}}\sum_i e^{i\mathbf{K}\cdot[\mathbf{R}_i+\boldsymbol{\tau}_B]}|p_z,i,B\rangle \\
|K'_A\rangle &= \frac{1}{\sqrt{N}}\sum_i e^{i\mathbf{K}'\cdot[\mathbf{R}_i+\boldsymbol{\tau}_A]}|p_z,i,A\rangle \\
|K'_B\rangle &= \frac{1}{\sqrt{N}}\sum_i e^{i\mathbf{K}'\cdot[\mathbf{R}_i+\boldsymbol{\tau}_B]}|p_z,i,B\rangle
\end{aligned} \tag{B1}$$

where A and B represent the A/B sublattices of graphene while K and K$'$ represent the two valleys with $\mathbf{K}(\mathbf{K}') = \frac{2\pi}{a}(\pm\frac{2}{3\sqrt{3}}, 0)$ and a being the distance between two nearest carbon atoms. $|p_z, i, A(B)\rangle$ is the p_z orbital of carbon atom centered at $\mathbf{R}_i + \boldsymbol{\tau}_{A(B)}$ denoting the position of the A(B) site in the i-th unit cell.

For top adsorption, the system possesses the symmetry represented by C_{3v} point group with the rotation center locating at the adsorption site assumed as A site. The symmetry operators in C_{3v} can be classified into three classes. The first class is the invariant operation labelled by $\hat{e}$ while the second class is rotation operation around z-direction by $2\pi/3$ ($4\pi/3$) denoted by $\hat{C}_3$ ($\hat{C}_3^2$). The third class is the mirror reflection about the three planes through rotation center labelled by $\hat{\sigma}_v$.[48] The generating operators are set as $\hat{C}_3$ and y-direction reflection $\hat{\sigma}_v$ which can be expressed as the following matrices on the basis of $|K_A\rangle$, $|K_B\rangle$, $|K'_A\rangle$, and $|K'_B\rangle$ that form a reducible four dimensional representation T_1,

$$\begin{aligned}
T_1(\hat{C}_3) &= \mathrm{diag}\{1, \omega, 1, \omega^*\} \\
T_1(\hat{\sigma}_v) &= \begin{pmatrix} 0 & 0 & 1 & 0 \\ 0 & 0 & 0 & 1 \\ 1 & 0 & 0 & 0 \\ 0 & 1 & 0 & 0 \end{pmatrix}
\end{aligned} \tag{B2}$$

where diag indicates a diagonal matrix with $\omega = e^{i2\pi/3}$. These matrices can be block diagonalized by a uniform

TABLE II: Symmetrized matrices and corresponding tensor operators for each block of effective Hamiltonian for top adsorption with C_{3v} symmetry. A_1, A_2, and E represents the irreducible representations of C_{3v} point group. M_{ij} is a 4×4 matrix with only one nonzero element locates at the i-th row and j-th column. Ladder operators $\sigma_{+,-}=\sigma_x\pm i\sigma_y$ with $\sigma_{x,y,z}$ being Pauli matrices. $\Delta_{\rm t}$ is constant, $\pi=k_x+ik_y$, and $k^2=k_x^2+k_y^2$.

Blocks	Representation	Symmetrized matrices	Tensor operator
$H_{A_1A_1}$ $H_{A_2A_2}$	$A_1\times A_1=$ $A_2\times A_2=A_1$	1	$\Delta_{\rm t}, k^2$
$H_{A_1A_2}$	$A_1\times A_2=A_2$	1	0
H_{A_1E}	$A_1\times E=E$	$\{M_{13},-M_{14}\}$	$\{\pi,\pi^\dagger\}$
H_{A_2E}	$A_2\times E=E$	$\{M_{23},M_{24}\}$	$\{\pi,\pi^\dagger\}$
H_{EE}	$E\times E=$ A_1+A_2+E	$A_1:\mathbf{1}_{2\times2}$ $A_2:\sigma_z$ $E:\{\sigma_+,-\sigma_-\}$	$A_1:\Delta_{\rm t},k^2$ $A_2:0$ $E:\{\pi,\pi^\dagger\}$

transformation that changes these basis into a new set of basis

$$\begin{pmatrix}|A_+\rangle\\|A_-\rangle\\|K_B\rangle\\|K'_B\rangle\end{pmatrix}=\begin{pmatrix}1/\sqrt{2}&0&1/\sqrt{2}&0\\1/\sqrt{2}&0&-1/\sqrt{2}&0\\0&1&0&0\\0&0&0&1\end{pmatrix}\begin{pmatrix}|K_A\rangle\\|K_B\rangle\\|K'_A\rangle\\|K'_B\rangle\end{pmatrix}. \tag{B3}$$

The corresponding matrix representation of these operators can be rewritten as

$$\begin{aligned}T_2(\hat{C}_3)&=\mathrm{diag}\{1,1,\omega,\omega^*\}\\T_2(\hat{\sigma}_v)&=\begin{pmatrix}1&0&0&0\\0&-1&0&0\\0&0&0&1\\0&0&1&0\end{pmatrix}\end{aligned} \tag{B4}$$

which indicates that $|A_+\rangle$ and $|A_-\rangle$ forms two inequivalent one-dimensional irreducible representations labelled by A_1 and A_2 corresponding to the split conduction band edges in Fig. 2(b). Moreover, $\{|K_B\rangle,|K'_B\rangle\}$ form a two-dimensional irreducible representation labelled by E that leads to the double degenerate valence band edges or crossing point shown in Fig. 2.

Based on these three irreducible representations, we can divide the effective Hamiltonian into nine blocks as follows according to the invariant expansion method introduced in Ref. [49]:

$$H_{\rm eff}=\begin{pmatrix}H_{A_1A_1}&H_{A_1A_2}&H_{A_1E}\\H_{A_2A_1}&H_{A_2A_2}&H_{A_2E}\\H_{EA_1}&H_{EA_2}&H_{EE}\end{pmatrix} \tag{B5}$$

where $H_{\alpha\beta}$ is a $D_\alpha\times D_\beta$ matrix with $D_\alpha(D_\beta)$ being the dimension of irreducible representation α (β). In order to obtain the effective Hamiltonian, we list in Tab. II the symmetrized matrices for each block and the corresponding tensor operators composed by momentum operators. Each block can be obtained by the production of symmetrized matrix and tensor operators.[49] Therefore, the effective Hamiltonian of can be expressed as

$$H_{\rm eff}=\begin{pmatrix}\Delta_{1\rm t}&0&\eta_{1\rm t}\pi^\dagger&-\eta_{1\rm t}\pi\\0&\Delta_{2\rm t}&\eta_{2\rm t}\pi^\dagger&\eta_{2\rm t}\pi\\\eta^*_{1\rm t}\pi&\eta^*_{2\rm t}\pi&\Delta_{3\rm t}&\eta_{3\rm t}\pi^\dagger\\\eta^*_{1\rm t}\pi^\dagger&\eta^*_{2\rm t}\pi^\dagger&-\eta_{3\rm t}\pi&\Delta_{3\rm t}\end{pmatrix} \tag{B6}$$

where $\pi=k_x+ik_y$ while $\Delta_{i\rm t}$ and $\eta_{i\rm t}$ (i = 1-3) are coupling constants and are complex numbers in general with $\eta^*_{i\rm t}$ being corresponding conjugate number and subscript t indicating top adsorption. In addition, due to the Hermiticity of Hamiltonian, $\eta^*_{3\rm t}=-\eta_{3\rm t}$ indicates that $\eta_{3\rm t}$ is a pure imaginary number. Finally, we can express this effective Hamiltonian in the basis of $|K_A\rangle$, $|K_B\rangle$, $|K'_A\rangle$, and $|K'_B\rangle$ as following by a unitary transformation:

$$H^{\rm eff}_{\rm t}=\begin{pmatrix}\Delta_{A\rm t}&v_{\rm t}\pi^\dagger&\Delta_{AA\rm t}&-v_{\delta\rm t}\pi\\v^*_{\rm t}\pi&\Delta_{B\rm t}&v^*_{\delta\rm t}\pi&\eta_{3\rm t}\pi^\dagger\\\Delta_{AA\rm t}&v_{\delta\rm t}\pi^\dagger&\Delta_{A\rm t}&-v_{\rm t}\pi\\-v^*_{\delta\rm t}\pi^\dagger&\eta^*_{3\rm t}\pi&-v^*_{\rm t}\pi^\dagger&\Delta_{B\rm t}\end{pmatrix} \tag{B7}$$

where $\Delta_{A\rm t}=(\Delta_{1\rm t}+\Delta_{2\rm t})/2$, $\Delta_{B\rm t}=\Delta_{3\rm t}$, $\Delta_{AA\rm t}=(\Delta_{1\rm t}-\Delta_{2\rm t})/2$, $v_{\rm t}=(\eta_{1\rm t}+\eta_{2\rm t})/\sqrt{2}$, and $v_{\delta\rm t}=(\eta_{1\rm t}-\eta_{2\rm t})/\sqrt{2}$. This Hamiltonian has the same form as Eq. (4).

For hollow adsorption, the system has C_{6v} symmetry with the rotation center locating at the adsorption site. For this case, we find that the four basis functions can be reconstructed into two two-dimensional irreducible representations as below:

$$\begin{aligned}|m_1\rangle&=(|K_B\rangle-|K'_A\rangle)/\sqrt{2}\\|m_2\rangle&=(|K_A\rangle-|K'_B\rangle)/\sqrt{2}\\|p_1\rangle&=(|K_B\rangle+|K'_A\rangle)/\sqrt{2}\\|p_2\rangle&=(|K_A\rangle+|K'_B\rangle)/\sqrt{2}\end{aligned} \tag{B8}$$

where the former (latter) two basis give rise an irreducible representation that is odd (even) under rotation of π. Therefore, we can divide the effective Hamiltonian into 4 blocks and each block is a 2×2 matrix that can be written as follows in the first order of momentum:

$$H_{\rm eff}=\begin{pmatrix}\Delta_{1\rm h}\mathbf{1}_{2\times2}&\eta_{\rm h}(k_x\sigma_x-k_y\sigma_y)\\\eta^*_{\rm h}(k_x\sigma_x-k_y\sigma_y)&\Delta_{2\rm h}\mathbf{1}_{2\times2}\end{pmatrix}. \tag{B9}$$

where the diagonal terms lead to two double degenerate energy levels which are separately conduction and valence band edges split by a gap of $|\Delta_{1\rm h}-\Delta_{2\rm h}|$ with subscript representing hollow adsorption. This Hamiltonian can be expressed on the basis of $|K_A\rangle$, $|K_B\rangle$, $|K'_A\rangle$, and $|K'_B\rangle$ as follows:

$$\begin{aligned}H^{\rm eff}_{\rm h}&=\frac{\Delta_{1\rm h}+\Delta_{2\rm h}}{2}\\&+\begin{pmatrix}0&v_{\rm h}\pi^\dagger&v_{\delta\rm h}\pi^\dagger&\Delta_{\rm h}\\v_{\rm h}\pi&0&\Delta_{\rm h}&v_{\delta\rm h}\pi\\v^*_{\delta\rm h}\pi&\Delta_{\rm h}&0&-v_{\rm h}\pi\\\Delta_{\rm h}&v^*_{\delta\rm h}\pi^\dagger&-v_{\rm h}\pi^\dagger&0\end{pmatrix}\end{aligned} \tag{B10}$$

where $\Delta_{\rm h} = \Delta_{\rm 2h} - \Delta_{\rm 1h}$, $v_{\rm h} = 2{\rm Re}(\eta_{\rm h})$, and $v_{\delta{\rm h}} = 2i{\rm Im}(\eta_{\rm h})$ with Re (Im) indicating the real (imaginary) part of a complex number. It is noted that, there is no staggered sublattice potential here due to inversion symmetry.

For bridge adsorption, we can also obtain the effective Hamiltonian similarly. However, this effective Hamiltonian is very complex since the symmetry of this system is lower than the previous ones. For simplicity, we divide the system into two parts where the first part is effective Hamiltonian of pristine graphene with D_{6h} symmetry and the second part account for the effects of adatoms with C_{2v} symmetry. The second part is treated as perturbation with only the lowest order contribution being included. We find that the four degenerate basis functions in pristine graphene can be reconstructed into four one dimensional presentations with the corresponding basis are

$$\begin{aligned} |mm\rangle &= (|K_B\rangle - |K'_A\rangle - |K_A\rangle + |K'_B\rangle)/2 \\ |pm\rangle &= (|K_B\rangle + |K'_A\rangle - |K_A\rangle - |K'_B\rangle)/2 \\ |mp\rangle &= (|K_B\rangle - |K'_A\rangle + |K_A\rangle - |K'_B\rangle)/2 \\ |pp\rangle &= (|K_B\rangle + |K'_A\rangle + |K_A\rangle + |K'_B\rangle)/2, \end{aligned} \tag{B11}$$

where the left (right) m/p indicates that the wavefunction is odd/even under rotation of π (y-direction reflection). We can obtain the effective Hamiltonian in the zeroth order of momentum that can be written as

$$H_{\rm eff} = {\rm diag}\{\Delta_{\rm 1b}, \Delta_{\rm 2b}, \Delta_{\rm 3b}, \Delta_{\rm 4b}\} \tag{B12}$$

where $\Delta_{i\rm b}$ (i = 1-4) are constants with subscript b indicating bridge adsorption. Then we express the effective Hamiltonian as follows under the basis of $|K_A\rangle$, $|K_B\rangle$, $|K'_A\rangle$, and $|K'_B\rangle$

$$\begin{aligned} H_{\rm b}^{\rm eff} &= v_F(\tau_z k_x \sigma_x + k_y \sigma_y) + \frac{\Delta_{\rm 11b}}{4}\mathbf{1}_{4\times 4} \\ &+ \frac{1}{4}\begin{pmatrix} 0 & \Delta_{\rm 21b} & \Delta_{\rm 31b} & \Delta_{\rm 41b} \\ \Delta_{\rm 21b} & 0 & \Delta_{\rm 41b} & \Delta_{\rm 31b} \\ \Delta_{\rm 31b} & \Delta_{\rm 41b} & 0 & \Delta_{\rm 21b} \\ \Delta_{\rm 41b} & \Delta_{\rm 31b} & \Delta_{\rm 21b} & 0 \end{pmatrix} \end{aligned} \tag{B13}$$

where $\Delta_{\rm 11b} = \sum_i \Delta_{i\rm b}$ with i = 1-4, $\Delta_{\rm 21b} = -\Delta_{\rm 1b} - \Delta_{\rm 2b} + \Delta_{\rm 3b} + \Delta_{\rm 4b}$, $\Delta_{\rm 31b} = \Delta_{\rm 1b} - \Delta_{\rm 2b} - \Delta_{\rm 3b} + \Delta_{\rm 4b}$, and $\Delta_{\rm 41b} = -\Delta_{\rm 1b} + \Delta_{\rm 2b} - \Delta_{\rm 3b} + \Delta_{\rm 4b}$. Here, staggered sublattice potential is absent similar to hollow adsorption and $\Delta_{\rm 31b}$ corresponds to the on-site potential induced intervalley coupling while $\Delta_{\rm 31b,41b}$ are induced by hopping term modification that is neglected in Sec. IV.

* Correspondence author: qiao@ustc.edu.cn

1. I. Žutić, J. Fabian, and S. Das Sarma, Rev. Mod. Phys. **76**, 323 (2004).
2. S.-Q. Shen, AAPPS Bulletin **18**, 29 (2008).
3. P. Seneor, B. Dlubak, M.-B. Martin, A. Anane, H. Jaffres, and A. Fert, MRS Bulletin **37**, 1245 (2012).
4. A. K. Geim and K. S. Novoselov, Nature Mater. **6**, 183-191 (2007).
5. A. H. Castro Neto, F. Guinea, N. M. R. Peres, K. S. Novoselov, and A. K. Geim, Rev. Mod. Phys. **81**, 109 (2009).
6. C. L. Kane and E. J. Mele, Phys. Rev. Lett. **95**, 226801 (2005).
7. Z. Qiao, W.-K. Tse, H. Jiang, Y. Yao, and Q. Niu, Phys. Rev. Lett. **107**, 256801 (2011).
8. A. Rycerz, J. Tworzydło, and C. W. J. Beenakker, Nature Phys. **3**, 172 (2007).
9. F. Guinea, M. I. Katsnelson, and A. K. Geim, Nature Phys. **6**, 30-33 (2010).
10. J. Li, I. Martin, M. Büttiker, and A. F. Morpurgo, Nature Phys. **7**, 38-42 (2011).
11. D. Pesin and A. H. MacDonald, Nature Mater. **11**, 409-416 (2012).
12. A. F. Morpurgo and F. Guinea, Phys. Rev. Lett. **97**, 196804 (2006).
13. M. Z. Hasan and C. L. Kane, Rev. Mod. Phys. **82**, 3045 (2010).
14. G. W. Semenoff, Phys. Rev. Lett. **53**, 2449 (1984).
15. S. Datta and B. Das, Appl. Phys. Lett. **56**, 665 (1990).
16. Z. Qiao, S. A. Yang, W. Feng, W.-K. Tse, J. Ding, Y. Yao, J. Wang, and Q. Niu, Phys. Rev. B **82**, 161414(R) (2010).
17. C. Weeks, J. Hu, J. Alicea, M. Franz, and R. Q. Wu, Phys. Rev. X **1**, 021001 (2011).
18. J. Hu, J. Alicea, R. Q. Wu, and M. Franz, Phys. Rev. Lett. **109**, 266801 (2012).
19. H. Zhang, C. Lazo, S. Blügel, S. Heinze, and Y. Mokrousov, Phys. Rev. Lett. **108**, 056802 (2012).
20. J. Ding, Z. Qiao, W. Feng, Y. Yao, and Q. Niu, Phys. Rev. B **84**, 195444 (2011).
21. V. V. Cheianov, V.I.Fal'ko, O. Syljuåsen, and B. L. Altshuler, Solid State Commun. **149**, 1499 (2009).
22. J. Jung, A. Raoux, Z. H. Qiao, and A. H. MacDonald, Phys. Rev. B **89**, 205414 (2014).
23. See more details in Appendix.
24. A. A. Abrikosov and S. D. Beneslavskii, J. Low Temp. Phys. **5**, 141 (1971).
25. H. Min, G. Borghi, M. Polini, and A. H. MacDonald, Phys. Rev. B **77**, 041407(R) (2008).
26. J. Jung, F. Zhang, and A. H. MacDonald, Phys. Rev. B **83**, 115408 (2011).
27. F. Zhang, J. Jung, G. A. Fiete, Q. Niu, and A. H. MacDonald, Phys. Rev. Lett. **106**, 156801 (2011).
28. D. Xiao, W. Yao, and Q. Niu, Phys. Rev. Lett. **99**, 236809 (2007).
29. J. M. Murray and O. Vafek, Phys. Rev. B **89**, 201110(R) (2014).
30. K. A. Pawlak, J. M. Murray, and O. Vafek, arXiv:1411.3633.
31. J. Velasco Jr, L. Jing, W. Bao, Y. Lee, P. Kratz, V. Aji, M. Bockrath, C. N. Lau, C. Varma, R. Stillwell, D. Smirnov, F. Zhang, J. Jung, and A. H. MacDonald, Nature Nanotech. **7**, 156-160 (2012).
32. K. S. Novoselov, E. McCann, S. V. Morozov, V. I. Fal'ko, M. I. Katsnelson, U. Zeitler, D. Jiang, F. Schedin, and A.

K. Geim, Nature Phys. **2**, 177 (2006).
[33] H. X. Yang, A. Hallal, D. Terrade, X. Waintal, S. Roche, and M. Chshiev, Phys. Rev. Lett. **110**, 046603 (2013).
[34] H. Huang, D. Wei, J. Sun, S. Wong, Y. P. Feng, A. H. C. Neto, and A. T. S. Wee, Sci. Rep. **2**, 983 (2012).
[35] L. Chen, C. Liu, B. Feng, X. He, P. Cheng, Z. Ding, S. Meng, Y. Yao, and K. Wu, Phys. Rev. Lett. **109**, 056804 (2012).
[36] M. Nishizawa, T. Eguchi, T. Misima, J. Nakamura, and T. Osaka, Phys. Rev. B **57**, 6317 (1998).
[37] Z. F. Wang, Z. Liu, and F. Liu, Phys. Rev. Lett. **110**, 196801 (2013).
[38] C.-H. Park and S. G. Louie, Nano Lett. **9**, 1793 (2009).
[39] C. Wu, D. Bergman, L. Balents, and S. Das Sarma, Phys. Rev. Lett. **99**, 070401 (2007).
[40] J.-Y. Yea, V. Mizeikisb, Y. Xua, S. Matsuoa, and H. Misawa, Opt. Commun. **211**, 205 (2002).
[41] J. Jin, *The finite element method in electromagnetics, 2nd ed.* (Wiley, 2002).
[42] J. D. Joannopoulos, S. G. Johnson, J. N. Winn, and R. D. Meade, *Photonic Crystals: Molding the Flow of Light* (Princeton Univ. Press, 2008).
[43] C. Ouyang, Z. Xiong, F. Zhao, B. Dong, X. Hu, X. Liu, and J. Zi, Phys. Rev. A **84**, 015801 (2011).
[44] R. Winkler, *Spin-orbit coupling effects in two-dimensional electron and hole systems* (Springer, Berlin, 2003).
[45] C. J. Tabert and E. J. Nicol, Phys. Rev. Lett. **110**, 197402 (2013).
[46] A. Pachoud, A. Ferreira, B. Özyilmaz, and A. H. Castro Neto, Phys. Rev. B **90**, 035444 (2014).
[47] J. R. Wallbank, M. Mucha-Kruczyński, and V. I. Fal'ko, Phys. Rev. B **88**, 155415 (2013).
[48] M. El-Batanouny and F. Wooten, *Symmetry and condensed matter physics: A computational approach* (Cambridge Univ. Press, 2008).
[49] R. Winkler and U. Zülicke, Phys. Rev. B **82**, 245313 (2010).